AGU ADVANCING EARTH AND SPACE SCIENCE

JGR Earth Surface

RESEARCH ARTICLE
10.1029/2022JF006898

Comprehensive Radar Mapping of Malaspina Glacier (Sít' Tlein), Alaska—The World's Largest Piedmont Glacier—Reveals Potential for Instability

B. S. Tober[1], J. W. Holt[1,2], M. S. Christoffersen[2], M. Truffer[3,4], C. F. Larsen[3], D. J. Brinkerhoff[5], and S. A. Mooneyham[6]

[1]Department of Geosciences, University of Arizona, Tucson, AZ, USA, [2]Lunar and Planetary Laboratory, University of Arizona, Tucson, AZ, USA, [3]Geophysical Institute, University of Alaska Fairbanks, Fairbanks, AK, USA, [4]Department of Physics, University of Alaska Fairbanks, Fairbanks, AK, USA, [5]Department of Computer Science, University of Montana, Missoula, MT, USA, [6]School of Geography, Development, and Environment, University of Arizona, Tucson, AZ, USA

Abstract Malaspina Glacier, located on the coast of southern Alaska, is the world's largest piedmont glacier. A narrow ice-cored foreland zone undergoing rapid thermokarst erosion separates the glacier from the relatively warm waters of the Gulf of Alaska. Glacier-wide thinning rates for Malaspina are greater than 1 m/yr, and previous geophysical investigations indicated that bed elevation exceeds 300 m below sea level in some places. These observations together give rise to the question of glacial stability. To address this question, glacier evolution models are dependent upon detailed observations of Malaspina's subglacial topography. Here, we map 2,000 line-km of the glacier's bed using airborne radar sounding data collected by NASA's Operation IceBridge. When compared to gridded radar measurements, we find that glaciological models overestimate Malaspina's volume by more than 30%. While we report a mean bed elevation 100 m greater than previous models, we find that Malaspina inhabits a broad basin largely grounded below sea level. Several subglacial channels dissect the glacier's bed: the most prominent of these channels extends at least 35 km up-glacier from the terminus toward the throat of Seward Glacier. Provided continued foreland erosion, an ice-ocean connection may promote rapid retreat along these overdeepened subglacial channels, with a global sea-level rise potential of 1.4 mm.

Plain Language Summary At the corner of southern Alaska, Malaspina Glacier spills out onto a broad coastal plain from the St. Elias Mountains. A thin land barrier separates Malaspina Glacier from the relatively warm waters of the Gulf of Alaska. Clean ice is exposed beneath vegetation at the edges of numerous water bodies across this barrier. Historical satellite imagery show these water bodies expanding over time, with a lagoon system even forming directly in front of the glacier over the past few decades. Airborne radar sounding allows us to map the glacier's bed in detail, demonstrating that the glacier sits largely below sea level and is cut by several channels at its bed that extend at least 35 km up-glacier. The continued loss of Malaspina's coastal barrier may provide pathways for ocean waters to access large areas of the glacier's bed along these channels. Assuming this leads to large-scale calving and the glacier's retreat, Malaspina has the potential to contribute 560 km^3 of ice, or 1.4 mm, to global sea-level rise.

Key Points:

- Two-thirds of Malaspina Glacier is grounded below sea level, and the piedmont's ice volume contains a sea-level rise potential of 1.4 mm
- The glacier's bed is cut by several subglacial channels where elevation reaches more than 350 m below sea level
- Bed topography is likely influenced by regional faulting, and drives surface topography, subglacial water drainage, and ice discharge

Supporting Information:

Supporting Information may be found in the online version of this article.

Correspondence to:

B. S. Tober,
btober@arizona.edu

Citation:

Tober, B. S., Holt, J. W., Christoffersen, M. S., Truffer, M., Larsen, C. F., Brinkerhoff, D. J., & Mooneyham, S. A. (2023). Comprehensive radar mapping of Malaspina Glacier (Sít' Tlein), Alaska—The world's largest piedmont glacier—Reveals potential for instability. *Journal of Geophysical Research: Earth Surface*, *128*, e2022JF006898. https://doi.org/10.1029/2022JF006898

Received 31 AUG 2022
Accepted 13 FEB 2023
Corrected 11 MAR 2023

This article was corrected on 11 MAR 2023. See the end of the full text for details.

1. Introduction

Despite glacier thinning being extensively documented globally (Hugonnet et al., 2021; Zemp et al., 2019), measurements of ice thickness remain lacking and critical to understanding potential future glacial loss, sea-level rise contributions, and water resource implications (Millan et al., 2022). Alaskan glaciers in particular are melting at an average rate of nearly 1 m/yr, contributing a total of ~0.2 mm/yr to global sea-level rise (Arendt et al., 2002; Gardner et al., 2013; Hugonnet et al., 2021; Jacob et al., 2012; Larsen et al., 2015). Along the coast of southern Alaska, the Agassiz, Seward, and Marvine glacial tributaries coalesce to form Malaspina Glacier (originally named *Sít' Tlein*, meaning Big Glacier, by the indigenous Tlingit, Deur et al., 2015; Figure 1a). The Seward lobe comprises the majority of the piedmont and is sourced by the Seward Glacier, with its accumulation zone in the St. Elias Mountains (Sharp, 1951). With an area of 2,400 km^2, Malaspina is the world's largest piedmont-type glacier (Molnia, 2001), and it is thinning at a rate greater than 1 m/yr (Larsen et al., 2015; Muskett et al., 2008).

Malaspina Glacier is located along the transition from the Fairweather fault transform plate boundary to the Yakutat fold and thrust belt, leading to the offshore Pamplona zone, which actively accommodates accretion of

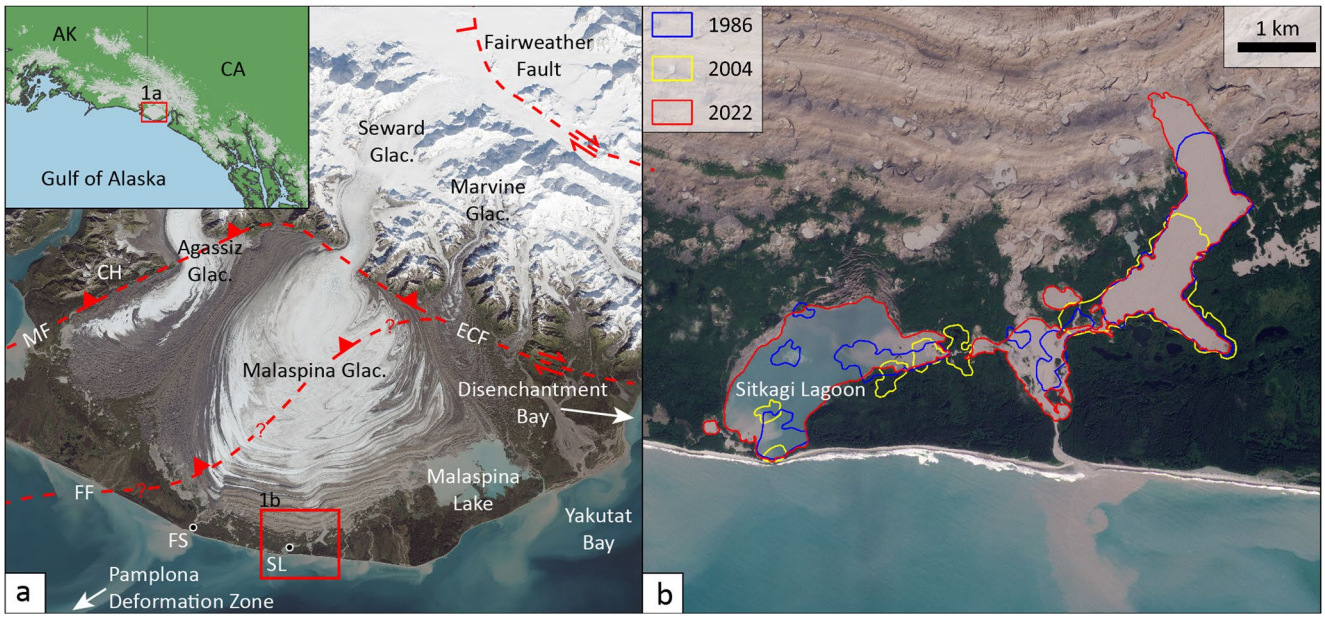

Figure 1. Study region overview. (a) The Agassiz, Seward, and Marvine glaciers feed their respectively named piedmont lobes, which together comprise Malaspina Glacier. Active faults are from Bruhn et al. (2012), where MF represents the Malaspina thrust fault, FF represents the Foreland thrust fault, and ECF represents the Esker Creek dextral-thrust fault. From west to east, faulting transitions from predominantly thrust type to dextral strike-slip as well as some oblique-slip. FS represents Fountain Stream, SL represents Sitkagi Lagoon, and CH represents Chaix Hills. 2014 basemap image courtesy of Landsat 8 Operational Land Imager. (b) Outlines of Sitkagi Lagoon and surrounding proglacial water bodies mapped in Landsat imagery, demonstrating foreland degradation and the growing potential for ocean water intrusion. 2022 basemap imagery courtesy of PlanetScope.

the Yakutat terrane to North America (Figure 1a; Bruhn et al., 2004, 2012; Pavlis et al., 2012; Plafker, 1987; Worthington et al., 2012). The Yakutat terrane converges with North America at a rate of ~50 mm/yr. Tectonic block models indicate that ~10 mm/yr of crustal shortening is accommodated along faults striking northeast beneath Malaspina Glacier from the Pamplona zone (Elliott et al., 2013). The onshore continuation of faults mapped offshore has previously remained unconfirmed due to their concealment by ice cover.

Although spatially limited, previous geophysical observations made by gravimetry, active seismic, and radar sounding demonstrate that Malaspina's bed extends to more than 300 m below sea level (Allen & Smith, 1953; Conway et al., 2009; Sharp, 1958; Truffer et al., 2016). Complex bed topography and an expansive subglacial drainage network are indicated by supraglacial valleys identified in both Landsat (Krimmel & Meier, 1975) as well as side-looking airborne radar (Molnia & Jones, 1989).

A narrow (<5 km wide) coastal foreland provides the glacier's only separation from the Gulf of Alaska, where summer surface water temperatures regularly surpass 10°C (NOAA station 46082; 46083). Thermokarst depressions along this barrier suggest that buried ice was abandoned during past glacial retreat. At the foreland's center, Sitkagi Lagoon has opened and grown to 3 km^2 over the past 50 years through ice cliff retreat (Figure 1b). Recent field measurements have confirmed the presence of saline water in Sitkagi Lagoon (Thompson et al., 2021). Just 2 km to the east, a proglacial lake has expanded from the glacier's foreland into debris-covered ice territory. Continued foreland wastage in this area may provide a pathway for warm ocean water intrusion to the glacier's terminus. The rapid tidewater glacier retreats experienced regionally since the end of the Little Ice Age at Columbia Glacier (Carlson et al., 2017), Icy Bay, and Glacier Bay (Post et al., 2011) have demonstrated that a tidewater glacier's stability is primarily dependent on its bed geometry (Pfeffer, 2007). While a tidewater Malaspina Glacier may differ significantly from these other systems, its subglacial topography will still dictate the extent and depths to which the ice front may be exposed to ocean water.

To address questions of glacial stability and geologic structure, we compile measurements from 2,000 line-km of airborne radar sounding profiles acquired by NASA's Operation IceBridge (OIB) into the first comprehensive and detailed map of Malaspina Glacier's bed.

2. Materials and Methods

2.1. NASA OIB Alaska Airborne Radar Sounding

Operation IceBridge annually acquired airborne laser altimetry measurements over ice masses in Alaska between 2009 and 2021, with the addition of radar sounding beginning in 2012 (MacGregor et al., 2021). Herein, we analyze 4,150 line-km of airborne radar sounding data acquired over Malaspina Glacier between 2013 and 2021.

Compared with radar sounders developed for use in Greenland and Antarctica (e.g., Moussessian et al., 2000; Shi et al., 2010), systems employed successfully in Alaska have operated at relatively low frequencies (e.g., Conway et al., 2009; Rignot et al., 2013) to better allow for radio wave penetration through Alaska's highly attenuating and scattering temperate ice masses (Watts & England, 1976). We present data acquired by impulse and linear frequency modulated (LFM) radar systems operating at center frequencies of 2.5 or 5 MHz, with vertical resolutions of 17 and 34 m in ice (Holt et al., 2021; M. Truffer et al., 2021; Table S1 in Supporting Information S1).

Clutter simulations are an essential auxiliary data set which allows subglacial bed returns to be discriminated from echoes produced by off-nadir surface topography, or "clutter" (Holt et al., 2006). These are generated to simulate radar surface returns for each profile as a function of aircraft trajectory and local topographic relief (Figure 2b). Clutter simulations were generated for all radar profiles using a regional digital elevation model (Kienholz et al., 2014). Herein, we omit radar measurements of Malaspina Glacier reported by Rignot et al. (2013) from the Warm Ice Sounder Experiment, as an analysis was not performed in that study to verify that interpreted bed echoes were not in fact clutter.

The vertical (range) resolution is often discussed in terms of the interpretation precision for a given radar sounder, defined by the ability to distinguish two signals close in time delay. While we report the theoretical vertical resolution of each radar system in Table S1 in Supporting Information S1, this system property is not equivalent to the precision of the radar-derived measurements presented herein. Interpretation precision is a combination of the quantization interval of bed echo interpretations, along with geometric (slope) errors, radar system timing, and positioning. The combined effect of these factors is best captured by analyzing the disagreement of intersecting radar profiles (Lapazaran et al., 2016), an analysis made particularly robust in this case by utilizing data from several instruments acquired over numerous field campaigns. We discuss this "crossover analysis" in Section 2.2.3.

2.2. Radar-Derived Bed Elevation and Ice Thickness

2.2.1. Along-Profile Measurements

Radar profiles over Malaspina Glacier were investigated using the Radar Analysis Graphical Utility (RAGU; Tober & Christoffersen, 2022). To discern suspected glacier bed returns from potential off-nadir surface returns, we qualitatively compared radar profiles with surface clutter simulations to ensure that the suspected bed returns were not mirrored by analogous surface returns modeled at a similar time-delay (Figures 2a–2c). While glacier bed returns can coincide in time with off-nadir surface returns, we are not able to disentangle these signals. To avoid any erroneous measurements, we therefore omit any radar returns which we cannot confidently qualify as a glacier bed return from our analysis.

Verified basal returns were manually digitized ("picked"), providing point-measurements along radar profiles of the two-way time delay from the radar sounder to the glacier bed (Figure 2c). Due to the flight altitude required by the laser altimeter employed by OIB in Alaska (300–500 m elevation above ground level; MacGregor et al., 2021), the glacier surface is typically not visible in linear frequency modulated radar profiles, as the instrument is still transmitting when the glacier surface echo is returned, saturating the receiver and obscuring the surface. Contemporaneous measurements of surface elevation from the onboard laser altimeter (Larsen, 2020) were therefore utilized to calculate glacier surface elevation at the time of the radar measurements. Englacial radar travel time delays were converted to depth by assuming a dielectric constant in water ice of 3.15 (wave speed of ∼169 m/μs; Evans, 1965). Elevations are reported as heights in reference to the WGS84 ellipsoid, which is locally ∼10 m below the local equipotential sea-level surface. The ground spacing of along-profile point-measurements is dependent on aircraft velocity, the radar pulse repetition frequency, and trace stacking, and is typically between 2 and 10 m.

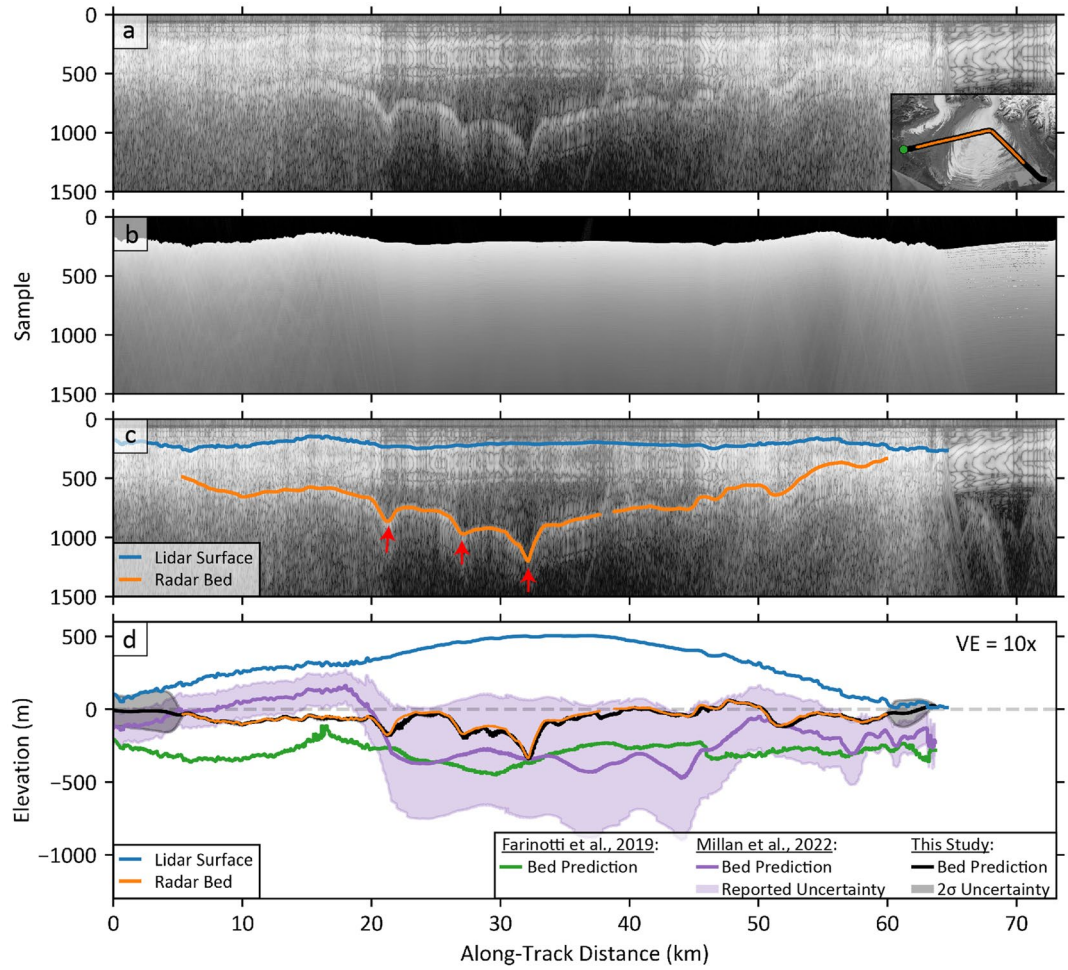

Figure 2. Representative radar profile across Malaspina Glacier. (a) Uninterpreted NASA OIB airborne radar sounding profile acquired over Malaspina Glacier by the Arizona Radio Echo Sounder operating at 2.5 MHz on 28 September 2019. (b) Corresponding clutter simulation. (c) Interpreted radar profile with lidar-derived surface (blue), manually picked glacier bed return (orange), and suspected subglacial channels (red arrows). (d) Along-profile comparison of the picked and modeled glacier bed, relative to ice thickness. Radar-derived bed elevation (orange) is compared to the modeled bed elevation (black) and corresponding 95% confidence interval (gray shading) of this study, and to the bed elevation obtained by subtracting global ice thickness models from the glacier's lidar-derived surface (blue). The corresponding bed elevation of Farinotti et al. (2019) is shown in green, with no reported uncertainty, while that of Millan et al. (2022), along with their reported uncertainty, is shown in purple. Gray horizontal dashed line indicates zero m elevation in reference to the WGS84 ellipsoid. Profile ground track is shown by black line in bottom right of panel (a), beginning to the west (green circle), with corresponding locations of the picked bed return in orange.

2.2.2. Radar Mapping

While many glaciers in Alaska present a great challenge to airborne radar sounding due to the combination of temperate ice and extreme surface clutter, Malaspina Glacier has proven an optimal target. Of the 4,150 line-km of radar sounding data acquired over Malaspina Glacier between 2013 and 2021, a distinct basal return is identified and mapped for 2,000 line-km (Figure S1 in Supporting Information S1). Topographic clutter is only apparent in radar profiles within several kilometers of the mouth of Seward Glacier and elsewhere along the piedmont's flanks. Profiles crossing the lobe transverse to the ice flow direction reveal several depressions cutting the glacier's bed (Figure 2c). Radar interpretations provide discrete measurements of bed elevation and ice thickness along profiles which parallel and cross each other in a grid pattern, with most profiles regularly spaced between 2 and 3 km.

2.2.3. Crossover Analysis

To assess interpretation bias, we compared radar-derived bed elevations from independent interpreter's bed picks along the same radar profiles. We find that the median (and interquartile range) in bed elevation disagreement between interpreters is 8 (12) m, corresponding to a median ice thickness disagreement of 2 (3) %.

As a more comprehensive means of assessing radar measurement uncertainty, bed elevations were compared at profile intersections by linearly interpolating between the two nearest points on each radar profile surrounding a given intersection. The difference between interpolated values for each profile represents the crossover disagreement. From the 702 profile crossings in this data set, the median (and interquartile range) crossover disagreement in bed elevation is 16 (19) m (Figure S2 in Supporting Information S1). Considering that this data set is the product of three different radar systems deployed over a time span of 8 years, this analysis reveals an extremely high degree of data consistency and interpretation reliability.

In theory, some bed elevation crossover disagreement may be explained by bedrock erosion taking place over this time period. Sediment yields—a proxy for erosion rate—for temperate glaciers in southeast Alaska are among the greatest recorded in the world, with glacier-wide values of up to 0.1 m/yr (Hallet et al., 1996), and local values as high as 3 m/yr (Motyka et al., 2006). Even considering those high rates would result in up to ∼20 m of Malaspina's bed having been eroded during the time period of this radar data acquisition, which would be barely detectable given our measurement uncertainty. Furthermore, crossover analysis revealed no correlation in the timespan between crossing profiles and the crossover disagreement in bed elevation. The disagreement we find through crossover analysis can be explained by the sources of error discussed in Section 2.1.

2.3. Measurement Interpolation

Discrete radar-derived bed elevations were interpolated through Gaussian process (GP) regression (Rasmussen & Williams, 2006). Bed elevation was modeled at desired locations as multivariate-normally distributed, with the covariance between points prescribed through a kernel function that assesses similarity as a function of proximity. The kernel is parameterized in terms of metrics such as the length scale at which elevations become uncorrelated, as well as the characteristic vertical scale of variability. Inferences about the bed elevation at unobserved locations are then made by conditioning this model upon known values at a collection of observed locations. The result of this procedure is a probability distribution over continuous bed elevations conditioned on observations, $P\left(\mathbf{b}(\mathbf{x})|\hat{\mathbf{b}}\right)$.

We use both radar-derived measurements and visible ice boundaries as observed points. Individual glacier outlines were acquired from the Global Land and Ice Measurements from Space database (GLIMS; Raup et al., 2007). Due to disagreement between the southern ice margin identified in recent satellite imagery and that outlined by GLIMS, this boundary was manually delineated by tracking changes in surface texture from an Interferometric Synthetic Aperture Radar (IFSAR) digital elevation model in context with satellite imagery (Thompson et al., 2023). Internal boundaries dividing the piedmont were removed and the resulting lobe outlines were treated as additional observations with elevation values given by IFSAR.

Kernel parameters were fit by maximizing the log-marginal likelihood, which identifies the parameter settings that render the observed data most probable under the chosen model. We performed this procedure for a handful of plausible kernels and found that the Matérn kernel (Rasmussen & Williams, 2006) produced the model in greatest agreement with observational data. Model predictions were made across a uniform grid covering the entire piedmont at a spatial resolution of 100 m resolution.

To maintain positive ice thickness, we further model the distribution over unknown bed elevations given surface elevations:

$$P\left(\mathbf{b}|\hat{\mathbf{b}},\hat{\mathbf{s}}\right) \propto P(\hat{\mathbf{s}}|\mathbf{b})P\left(\mathbf{b}|\hat{\mathbf{b}}\right) \tag{1}$$

where $P\left(\mathbf{b}|\hat{\mathbf{b}},\hat{\mathbf{s}}\right)$ is the posterior probability of unknown bed elevations ($\mathbf{b}$) given observations of both bed elevation ($\hat{\mathbf{b}}$) and surface elevation ($\hat{\mathbf{s}}$), and $P(\hat{\mathbf{s}}|\mathbf{b})$ is the likelihood of surface elevations conditioned on the bed

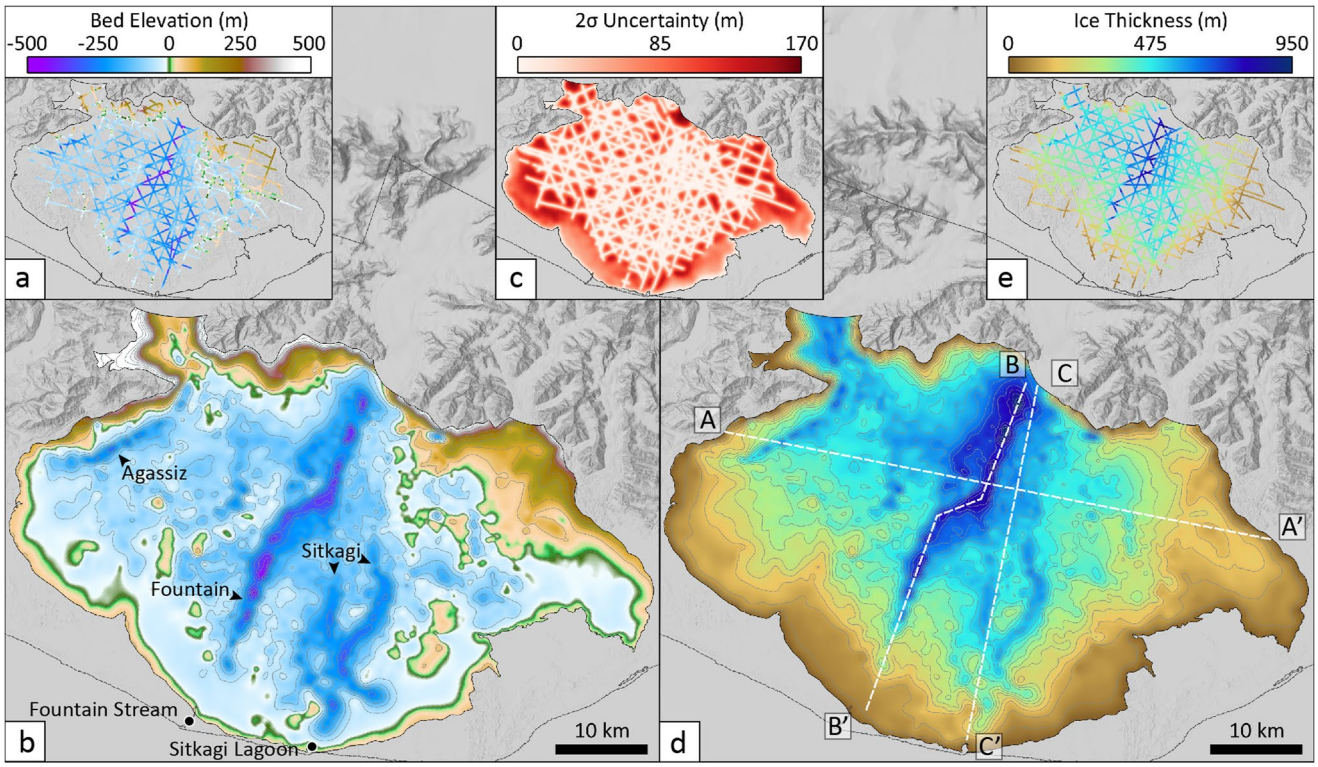

Figure 3. Malaspina Glacier bed elevation and ice thickness. (a) Along-profile bed elevation. (b) Interpolated bed elevation. Arrowheads denote Agassiz, Fountain, and Sitkagi subglacial channels. (c) 2σ uncertainty in interpolated bed elevation. (d) Interpolated ice thickness. Dashed lines illustrate the location of the cross-sectional glacier profiles shown in Figure 4. (e) Along-profile ice thickness. Bed elevations represent height in reference to the WGS84 ellipsoid, which is locally ∼10 m above equipotential sea level. The contour interval is 50 m for (b, d).

elevation. The likelihood used to constrain the model (Swiler et al., 2020) enforces the condition that negative ice thickness is highly improbable:

$$P(\hat{\mathbf{s}}|\mathbf{b}) \propto 0 \text{ if } (\hat{\mathbf{s}} - \mathbf{b}) < 0, 1 \text{ else} \tag{2}$$

This likelihood is non-conjugate with the Gaussian process, so we draw samples from Equation 1 using importance sampling.

This interpolation method yields a mean bed elevation as well as a marginal standard deviation. The interpolation uncertainty presented forthwith is two times this marginal standard deviation, which implies that the true bed lies within these bounds with approximately 95% probability. We note that while the mean bed provided by this model will be smoother than the glacier's true bed (e.g., MacKie et al., 2021), this interpolation approach produces a probability distribution over beds with variable roughness. Gridded measurements of ice thickness are achieved by subtracting modeled bed elevations from 2012 surface elevations provided by IFSAR.

3. Results and Discussion

3.1. Subglacial Topography and Glacier Thickness

Along-profile measurements of bed elevation clearly demonstrate that Malaspina Glacier is predominantly grounded below sea level (Figure 3a). Bed elevation exceeds 350 m below sea level within distinct basal troughs that line up between consecutive radar profiles and lead toward the glacier's terminal margin, alluding to a network of subglacial channels. Bed elevation remains at ∼400 m below sea level near the Seward throat, at the northernmost extent of our along-profile radar measurements. Gridded measurements provide for a detailed understanding of Malaspina's subglacial morphology and an assessment of ice thickness (Figures 3b and 3d).

A particularly well-defined channel follows a ∼35 km south-southwest path from the head of the Seward lobe toward Fountain Stream (henceforth named "Fountain Channel"), with a notable ∼5 km right-lateral offset at the glacier's center. Ten kilometers southeast of the glacier's center, two less defined channels meander ∼15 km

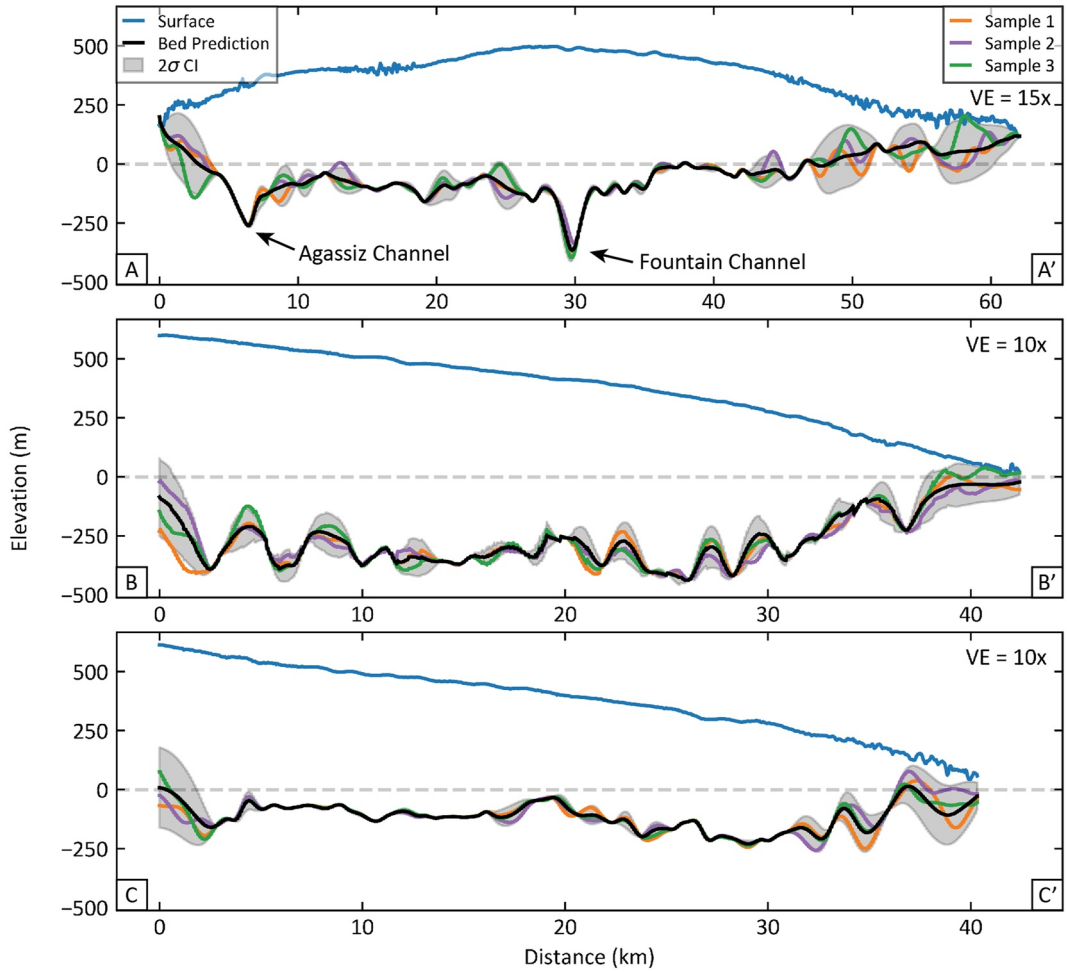

Figure 4. Probability densities of bed elevation relative to ice thickness along profiles (top) A-A′, (middle) B-B′, and (bottom) C-C′. Profile locations are shown by dashed white lines in Figure 3d. Blue line represents the glacier's surface elevation provided by IFSAR. Black line corresponds to the model bed prediction (mean bed), with the associated 2σ posterior credibility interval shaded in gray. Orange, purple, and green lines correspond to three random samples of the posterior distribution. Gray horizontal dashed line indicates zero m elevation in reference to the WGS84 ellipsoid. Subglacial channel crossings are apparent in profile A-A′. Profile B-B′ follows Fountain Channel from the throat of Seward Glacier toward Fountain Stream.

south-southeast toward the actively degrading Sitkagi Lagoon region ("Sitkagi Channels"). The upper reaches of these channels are separated from Fountain Channel by a 200 m rise in basal topography. Another channel follows a ∼15 km southwestward path beneath the Agassiz lobe toward Icy Bay ("Agassiz Channel"). Supraglacial valleys with up to ∼50 m of relief atop the Seward lobe mirror Fountain and Sitkagi channels, disrupting the otherwise convex surface (Figure S3 in Supporting Information S1; Cotton et al., 2014). We suggest that these surface valleys are effectively transferred from the glacier's bed, as greater stresses associated with thicker ice overlying subglacial channels lead to greater flow velocities and hence surface drawdown.

Owing to the dense spatial coverage of radar-derived measurements, the bed model presented herein demonstrates a high degree of confidence across Malaspina Glacier (Figures 3c and 4). The 2σ uncertainty in bed elevation along radar profiles is generally below 20 m, in agreement with our crossover analysis (Section 2.2.3). Model uncertainty increases to reach ∼150 m where data gaps exist between radar flightlines, moving up the trunk of each tributary glacier, and along the glacier's terminus. Data gaps along the glacier's terminus margin may obscure the continuation of Malaspina's subglacial channels toward the terminus (Figures 3a and 3b).

Random bed solutions taken from the posterior distribution have variable roughness yet are primarily confined to the uncertainty envelope surrounding the mean bed solution (Figure 4). Despite increased model uncertainty

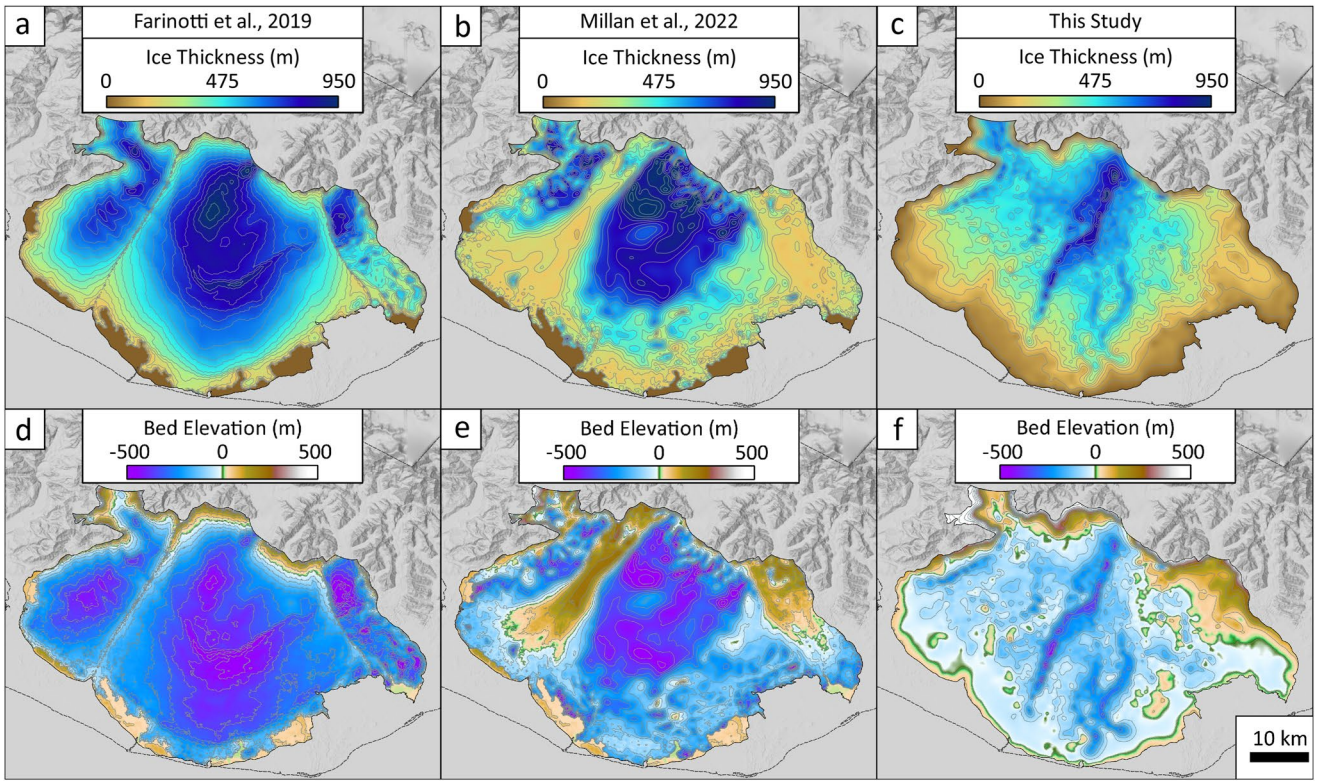

Figure 5. Comparison of modeled ice thickness and bed elevation between (a, d) Farinotti et al. (2019), (b, e) Millan et al. (2022), and (c, f) this study. Top panels represent ice thickness for each model, while bottom panels represent the accompanying bed elevation. The contour interval for each panel is 50 m.

along the glacier's margins, elevation profiles reveal an overdeepened bed geometry. Fountain Channel deepens by more than 300 m within 15 km from the glacier's toe (Figure 4b).

To assess how much of Malaspina's bed rests below sea level, the piedmont's volume, and its sea-level rise (SLR) potential, we randomly sampled 100,000 bed solutions from our Gaussian process posterior distribution and report the median (and interquartile range) of these metrics (Figure S4 in Supporting Information S1). We find that 1,390 (24) km^2, or 65 (1) %, of Malaspina's bed is grounded below sea level. Altogether, we report an ice volume of 691 (3) km^3 for the piedmont. Of this, 560 (2) km^3 is positioned above freeboard height, constituting a sea-level rise potential of 1.4 (<0.01) mm (S1; Figure S5 in Supporting Information S1).

We find that global models largely overestimate Malaspina Glacier's thickness (Figures 5a–5c and 6; Figure S6 in Supporting Information S1). In their global ice thickness consensus study, Farinotti et al. (2019) incorporate model results from several previous studies. The integrated thickness which Farinotti et al. (2019) present across the Malaspina piedmont results in a volume of 1,098 km^3, with no reported uncertainty. The individual models which are combined to provide this ice thickness estimate from Farinotti et al. (2019) either rely on the shallow ice approximation and invert estimated basal shear stress for ice thickness using observed surface slopes (Frey et al., 2014), or are based on principles of mass conservation and the shallow ice approximation (Huss & Farinotti, 2012; Maussion et al., 2019). In a more recent study, the integrated thickness which Millan et al. (2022) present for the Malaspina piedmont results in a volume of 907 km^3 with a total reported uncertainty of 237 km^3. The model presented by Millan et al. (2022) is an implementation of the shallow ice approximation which allows for basal sliding. Herein, after extensive sampling of the radar measurement-based probability distribution of bed solutions, we report a piedmont ice volume between 690 and 693 km^3. We note that while the volume calculated from the ice thickness model of Millan et al. (2022) is 31% greater than the value reported in this study, the ice volume we report does fall within their uncertainty range.

The overestimation of ice thickness clearly corresponds to greater predicted overall bed depths. However, comparing bed elevations between these various models is not so straightforward. As basal elevations were not

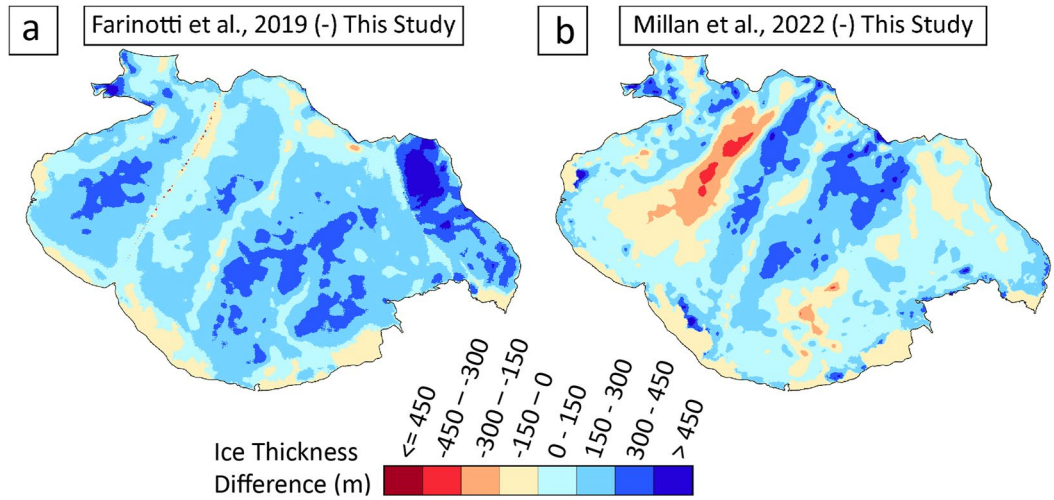

Figure 6. Difference in ice thickness obtained by (a) subtracting the ice thickness of Farinotti et al. (2019) from that of this study, and by (b) subtracting the ice thickness of Millan et al. (2022) from that of this study.

readily available from the models of Farinotti et al. (2019) or Millan et al. (2022), we subtract their ice thickness models from the same 2012 IFSAR surface elevation model used throughout this study (Figures 5d and 5e). We acknowledge that there is temporal disagreement between these various datasets. However, we expect that the implications of surface elevation changes between the periods of these studies are insignificant compared to the uncertainties associated with each individual model. Taking the presented thickness values from each study and subtracting from the IFSAR 2012 piedmont surface, we find a mean bed elevation of −225 m from the thickness model presented by Farinotti et al. (2019), and −135 m from the thickness model presented by Millan et al. (2022), compared with a mean bed elevation of −33 m for this study, and not considering individual model uncertainties. Perhaps more importantly, their bedrock reconstructions lack the very clear structural patterns with deep subglacial valleys that are revealed by our measurements (Figures 5d–5f). This has implications for the routing of subglacial water (see Section 3.3) and also for assessing potential retreat pathways.

We suspect that the discrepancy between Malaspina's "true" ice thickness and that presented by global models is a product of Malaspina Glacier's complexity (Figure 6). Being a surging glacier (Post, 1969), ice is primarily supplied across Malaspina through basal sliding, a mechanism which the traditional shallow ice approximation does not account for. While Millan et al. (2022) incorporate basal sliding into the shallow ice approximation in their model using the surface slope and averaged 2017–2018 surface velocities, the authors stress the issues with applying their method to surging glaciers. Using velocity data from a single year will likely only capture either the active or quiescent phase of a surging glacier, which will then lead to either an over- or underestimate of ice thickness, respectively. Glacier surface velocities generated using auto-RIFT (Gardner et al., 2018) and provided by the NASA MEaSUREs ITS_LIVE project (Gardner et al., 2022) demonstrate that this approach is particularly troublesome for Malaspina, as velocities vary greatly over time and in ways that are not spatially uniform across the piedmont (Figure S7 in Supporting Information S1).

Incorporating mass conservation is also not straightforward for Malaspina, as significant portions of the piedmont are debris-covered, therefore making it difficult to accurately quantify surface mass balance. The difference in ice volume between these studies and the improvement of our model uncertainty demonstrate the remaining necessity for measurements of ice thickness to further constrain thickness models, particularly for complex glacial systems such as the Malaspina.

3.2. Morphological Indications of Ice Flow

Offshore seismic data collected along the continental shelf margin and within neighboring Disenchantment and Yakutat bays provide evidence for glacial advance pathways which were activated repeatedly during past glacial periods (Elmore et al., 2013; Worthington et al., 2010; Zurbuchen et al., 2015). Elmore et al. (2013) suggest that Malaspina Glacier dominated the western portion of Yakutat Bay during past glacials, advancing southeast and joining Hubbard Glacier to flow toward the shelf along the Yakutat Sea Valley.

Subglacial topography mapped at Malaspina's bed may represent a signature of the glacier's flow history. While several subglacial channels are identified beneath the central and western portions of Malaspina Glacier, there is a notable lack of similar topographic features to the east. Moreover, modern observations of surface velocity indicate that ice emanating from Seward Glacier, Malaspina's primary tributary, is channelized and flows predominantly south-southwest along the path of Fountain Channel (Cotton et al., 2014). If current surface velocities and subglacial morphology together are indicative of past glacial flow conditions, the Malaspina may have followed a more direct route toward the shelf margin during past glacials.

3.3. Subglacial Drainage

Radar-derived measurements of ice thickness and bed elevation allow for an assessment of subglacial water drainage, which may have implications for Malaspina's flow dynamics (Davison et al., 2019). We calculate the hydraulic potential (ϕ) at the glacier's bed assuming that basal water pressure across the piedmont lobe is at a constant fraction of the ice overburden pressure. This results in $\phi = \rho_w g z + \kappa \rho_i g h$ where ρ_w represents the density of liquid water, z is bed elevation, κ is the ice flotation fraction representing the influence of ice overburden pressure on subglacial water pressure, ρ_i is the density of ice, h is ice thickness, and g is gravity (Shreve, 1972). In reality, an ever-evolving subglacial hydraulic system implies that the ice flotation fraction varies spatiotemporally, but here we choose a spatially constant value of κ to provide insight into the sensitivity of water routing with changes in κ. As with Zechmann et al. (2021), we compare subglacial water routing for hydraulic potential surfaces corresponding to ice flotation fractions of 0.50, 0.75, and 1.0. For each fractional ice flotation the D∞ flow accumulation algorithm (Tarboton, 1997) is used to determine subglacial drainage such that water is routed to the steepest down-gradient slope of the eight triangular facets centered on each grid cell of the hydraulic potential surface.

For all realizations of subglacial water routing produced for the range of ice flotation values tested herein, the predicted drainages share a strong first-order spatial correlation with subglacial topography (Figure 7). While hydraulic gradients are generally uniform across the piedmont's bed, indicating well-distributed flow, modeled subglacial flow pathways clearly correspond to Agassiz, Fountain, and Sitkagi channels. Bolstering this assessment, historical satellite imagery demonstrate that many of the modeled subglacial flow pathways terminate along the glacial forelands at the head of proglacial streams where high sediment flux is observed discharging into the Gulf of Alaska (Figure 7d; Figure S8 in Supporting Information S1). A prominent subglacial flow pathway follows Fountain Channel, terminating at the head of Fountain Stream, while another follows Agassiz Channel and terminates at the head of a proglacial stream that empties into Icy Bay. The emergence of pressurized water at the head of Fountain Stream was already noted in the earliest description of the glacier that we are aware of Russell (1893). Modeled subglacial drainages also largely mirror the Sitkagi subglacial channel system, with the western drainage branch feeding a proglacial stream between Sitkagi Lagoon and an adjacent proglacial lake to the east (Figure 1b). We suspect that the arrangement of subglacial discharge of water and sediment will be important to the continued evolution of Malaspina's foreland. With the lack of Malaspina's prominent subglacial valleys that are revealed by our measurements being captured in either the Farinotti et al. (2019) or Millan et al. (2022) thickness models, the indicated spatial pattern of subglacial discharge differs greatly from that expected based on the ice thickness and bed topography presented herein (Figure S9 in Supporting Information S1).

3.4. Geologic Controls

Potential geologic controls on the evolution of Malaspina Glacier are indicated by the correlation between subglacial morphology and regional faulting (Figure 7d). The path of Agassiz Channel matches that of the Malaspina thrust fault, which strikes northeast at the base of Chaix Hills (Chapman et al., 2012).We speculate that the 5 km right-lateral offset observed along Fountain Channel may be associated with the Foreland thrust fault, which strikes northeast from the Pamplona zone and is the deformation front of Yakutat-North America collision (Elliott et al., 2013; Gulick et al., 2013; Pavlis et al., 2012). This dogleg may be caused by an oblique slip component of deformation along the Foreland fault, matching the transform motion of faults along the eastern extent of the tectonic domain (Walton et al., 2022). Perhaps supporting this hypothesis, radar profiles crossing Fountain Channel reveal clear asymmetry in its cross-sectional shape, which may be a result of crustal shortening (Figure S10 in Supporting Information S1). While the morphology of Fountain and Agassiz channels share a notable relationship with regional faulting, there is no clear tectonic control for the morphology of Sitkagi Channels, as well as for the entire eastern extent of the glacier.

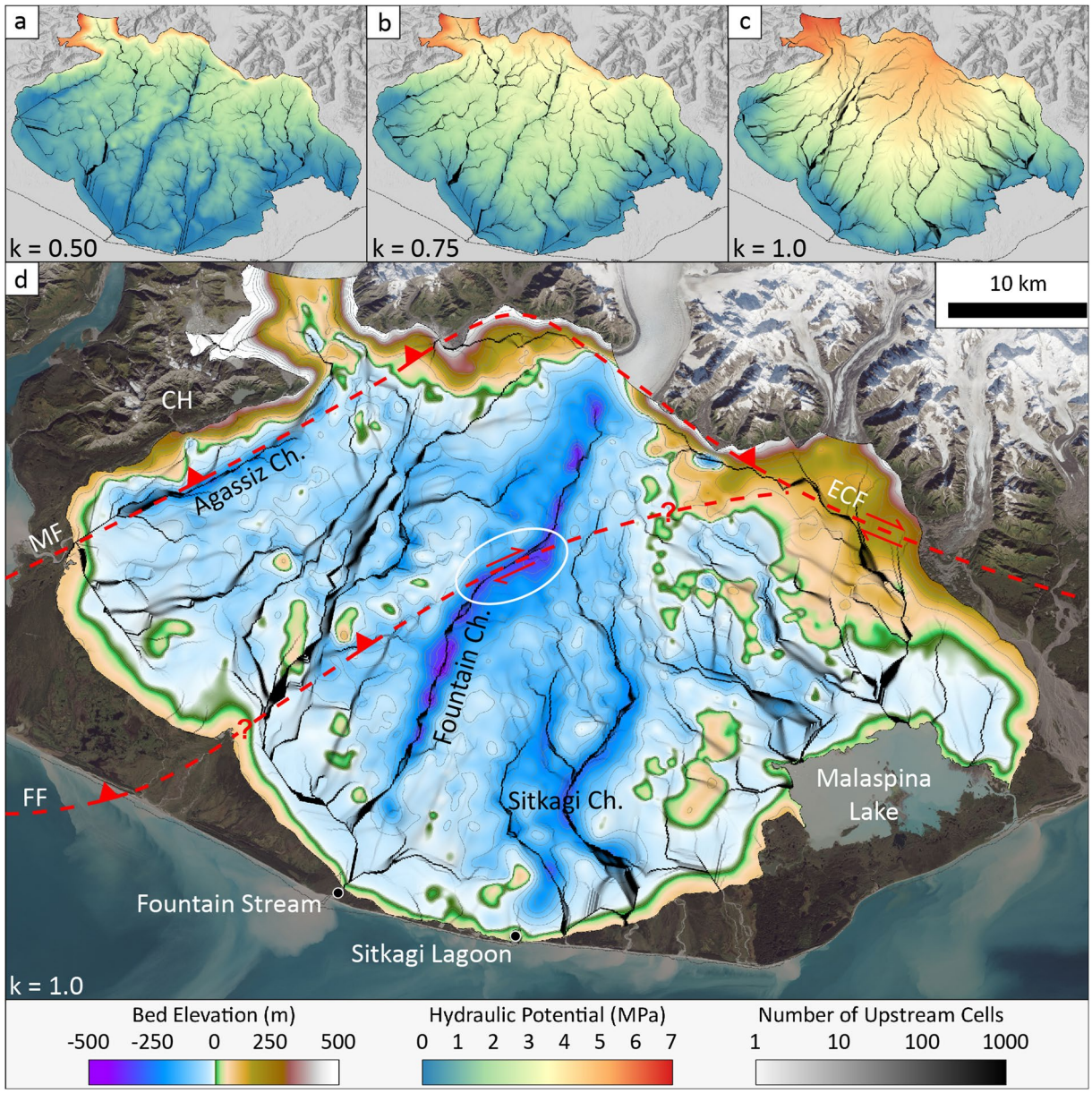

Figure 7. Relationship between subglacial topography, water drainage, and geologic structure. Black pathways represent modeled water routing across the subglacial hydraulic potential surface for an ice flotation factor of (a) $\kappa = 0.50$, (b) $\kappa = 0.75$, (c) $\kappa = 1.0$. (d) Subglacial flow pathways for $\kappa = 1.0$, in relation to subglacial topography, and local faulting. MF represents the Malaspina fault, FF represents the Foreland fault, and ECF represents the Esker Creek fault. Fault locations were modified from Bruhn et al. (2012), so that the Malaspina fault lines up with Agassiz Channel, and the Foreland Fault intersects the right-lateral offset in Fountain Channel (circled in white). 2014 basemap image courtesy of Landsat 8 Operational Land Imager.

4. Conclusions

Radar sounding data acquired over Malaspina Glacier as part of NASA's Operation IceBridge allow us to map 2,000 line-km of the glacier's bed. Interpolated measurements of ice thickness and bed elevation produced through Gaussian process regression provide a detailed understanding of the glacier's geometry. These data are accompanied by a robust measure of uncertainty and may serve as key components in accurately modeling the glacier's future evolution. Compared to interpolated radar measurements, we find that established ice thickness modeling approaches overestimate Malaspina's volume by 31%–59%. The discrepancy between the radar-derived ice thickness presented in this study and that of prior models demonstrates the continued need for measurements of ice thickness in constraining global ice volumes, and for accurately modeling future glacial evolution.

Malaspina's concave bed is largely grounded below sea level and is cut by several prominent subglacial channels. Fountain Channel in particular reaches 35 km up-glacier from the terminus, cutting the entire piedmont, and remains at 400 m below sea level near the throat of Seward Glacier. We consider channels at the bed of Malaspina Glacier to be controlled in part by regional faulting and suggest that the right-lateral offset observed along Fountain Channel may be related to oblique-slip along the Malaspina foreland thrust fault—the leading edge of the Yakutat-North America subduction zone. We find that subglacial drainages are generally well-distributed across the piedmont, following channels where they exist at the glacier's bed. The pattern of subglacial discharge is likely to contribute to the future evolution of Malaspina's ice-cored foreland and will thus impact the extent of ocean water intrusion to the glacier's terminus. Should ongoing foreland degradation and Malaspina's subglacial topography result in glacial retreat, Malaspina has the potential to contribute up to 1.4 mm to global sea-level rise.

Data Availability Statement

All NASA OIB Alaska lidar and radar data used in this work are available through the National Snow and Ice Data Center (https://doi.org/10.5067/AATE4JJ91EHC; https://doi.org/10.5067/Q0AVPHN3250H; https://doi.org/10.5067/X2H7MP5DBTYP). All radar picks were made using the Radar Analysis Graphical Utility (https://doi.org/10.5281/zenodo.6366661). Derived measurements of ice thickness, bed elevation, gridded products, and all code used to produce these interpolations, subglacial water flow models, and the figures accompanying this manuscript are available at University of Arizona's Research Data Repository (https://doi.org/10.25422/azu.data.17054063). IFSAR data used to produce a digital elevation model of the study area were collected by Fugro EarthData and acquired through the Elevation Portal of the Alaska Division of Geological and Geophysical Surveys (https://elevation.alaska.gov/).

Acknowledgments

The authors acknowledge Paul Claus and Ultima Thule Outfitters for providing the flight services that enabled acquisition of the data investigated herein. We thank Sean Gulick for contributing valuable insight into the connection between subglacial topography and regional geologic structure. We also thank Anna Thompson and Mike Loso for providing an improved delineation of the glacier's terminus. Seth Campbell and an anonymous reviewer provided valuable feedback which improved this manuscript. BT was funded by NASA's FINESST fellowship program, award 80NSSC19K1357. BT, JH, MC, MT, and CL were supported by Operation IceBridge Alaska, NASA award NNX16AC32G. All authors were supported by NSF award 1929566.

References

Allen, C. R., & Smith, G. I. (1953). Seismic and gravity investigations on the Malaspina Glacier, Alaska. *Eos, Transactions American Geophysical Union*, *34*(5), 755–760. https://doi.org/10.1029/TR034i005p00755

Arendt, A. A., Echelmeyer, K. A., Harrison, W. D., Lingle, C. S., & Valentine, V. B. (2002). Rapid wastage of Alaska glaciers and their contribution to rising sea level. *Science*, *297*(5580), 382–386. https://doi.org/10.1126/science.1072497

Bruhn, R. L., Pavlis, T. L., Plafker, G., & Serpa, L. (2004). Deformation during terrane accretion in the Saint Elias orogen, Alaska. *GSA Bulletin*, *116*(7–8), 771–787. https://doi.org/10.1130/B25182.1

Bruhn, R. L., Sauber, J., Cotton, M. M., Pavlis, T. L., Burgess, E., Ruppert, N., & Forster, R. R. (2012). Plate margin deformation and active tectonics along the northern edge of the Yakutat terrane in the Saint Elias orogen, Alaska, and Yukon, Canada. *Geosphere*, *8*(6), 1384–1407. https://doi.org/10.1130/GES00807.1

Carlson, A. E., Kilmer, Z., Ziegler, L. B., Stoner, J. S., Wiles, G. C., Starr, K., et al. (2017). Recent retreat of Columbia Glacier, Alaska: Millennial context. *Geology*, *45*(6), 547–550. https://doi.org/10.1130/G38479.1

Chapman, J. B., Pavlis, T. L., Bruhn, R. L., Worthington, L. L., Gulick, S. P. S., & Berger, A. L. (2012). Structural relationships in the eastern syntaxis of the St. Elias orogen, Alaska. *Geosphere*, *8*(1), 105–126. https://doi.org/10.1130/GES00677.1

Conway, H., Smith, B., Vaswani, P., Matsuoka, K., Rignot, E., & Claus, P. (2009). A low-frequency ice-penetrating radar system adapted for use from an airplane: Test results from Bering and Malaspina Glaciers, Alaska, USA. *Annals of Glaciology*, *50*(51), 93–97. https://doi.org/10.3189/172756409789097487

Cotton, M. M., Bruhn, R. L., Sauber, J., Burgess, E., & Forster, R. R. (2014). Ice surface morphology and flow on Malaspina Glacier, Alaska: Implications for regional tectonics in the Saint Elias orogen. *Tectonics*, *33*(4), 581–595. https://doi.org/10.1002/2013TC003381

Davison, B. J., Sole, A. J., Livingstone, S. J., Cowton, T. R., & Nienow, P. W. (2019). The influence of hydrology on the dynamics of land-terminating sectors of the Greenland Ice Sheet. *Frontiers of Earth Science*, *7*. https://doi.org/10.3389/feart.2019.00010

Deur, D., Thornton, T., Lahoff, R., & Hebert, J. (2015). *Yakutat Tlingit and Wrangell-St. Elias national park and preserve: An ethnographic overview and assessment*. Anthropology Faculty Publications and Presentations. Retrieved from https://pdxscholar.library.pdx.edu/anth_fac/99

Elliott, J., Freymueller, J. T., & Larsen, C. F. (2013). Active tectonics of the St. Elias orogen, Alaska, observed with GPS measurements. *Journal of Geophysical Research: Solid Earth*, *118*(10), 5625–5642. https://doi.org/10.1002/jgrb.50341

Elmore, C. R., Gulick, S. P. S., Willems, B., & Powell, R. (2013). Seismic stratigraphic evidence for glacial expanse during glacial maxima in the Yakutat Bay Region, Gulf of Alaska. *Geochemistry, Geophysics, Geosystems*, *14*(4), 1294–1311. https://doi.org/10.1002/ggge.20097

Evans, S. (1965). Dielectric properties of ice and snow–a review. *Journal of Glaciology*, *5*(42), 773–792. https://doi.org/10.3189/S0022143000018840

Farinotti, D., Huss, M., Fürst, J. J., Landmann, J., Machguth, H., Maussion, F., & Pandit, A. (2019). A consensus estimate for the ice thickness distribution of all glaciers on Earth. *Nature Geoscience*, *12*(3), 168–173. Article 3. https://doi.org/10.1038/s41561-019-0300-3

Frey, H., Machguth, H., Huss, M., Huggel, C., Bajracharya, S., Bolch, T., et al. (2014). Estimating the volume of glaciers in the Himalayan–Karakoram region using different methods. *The Cryosphere*, *8*(6), 2313–2333. https://doi.org/10.5194/tc-8-2313-2014

Gardner, A., Fahnestock, M., & Scambos, T. (2022). *MEaSUREs ITS_LIVE Landsat image-pair glacier and ice sheet surface velocities, version 1*. NASA National Snow and Ice Data Center Distributed Active Archive Center. https://doi.org/10.5067/IMR9D3PEI28U

Gardner, A. S., Moholdt, G., Cogley, J. G., Wouters, B., Arendt, A. A., Wahr, J., et al. (2013). A reconciled estimate of glacier contributions to sea level rise: 2003 to 2009. *Science*, *340*(6134), 852–857. https://doi.org/10.1126/science.1234532

Gardner, A. S., Moholdt, G., Scambos, T., Fahnstock, M., Ligtenberg, S., van den Broeke, M., & Nilsson, J. (2018). Increased West Antarctic and unchanged East Antarctic ice discharge over the last 7 years. *The Cryosphere*, *12*(2), 521–547. https://doi.org/10.5194/tc-12-521-2018

Gulick, S. P. S., Reece, R. S., Christeson, G. L., van Avendonk, H., Worthington, L. L., & Pavlis, T. L. (2013). Seismic images of the transition fault and the unstable Yakutat–Pacific–North American triple junction. *Geology*, *41*(5), 571–574. https://doi.org/10.1130/G33900.1

Hallet, B., Hunter, L., & Bogen, J. (1996). Rates of erosion and sediment evacuation by glaciers: A review of field data and their implications. *Global and Planetary Change*, *12*(1), 213–235. https://doi.org/10.1016/0921-8181(95)00021-6

Holt, J. W., Peters, M. E., Kempf, S. D., Morse, D. L., & Blankenship, D. D. (2006). Echo source discrimination in single-pass airborne radar sounding data from the Dry Valleys, Antarctica: Implications for orbital sounding of Mars. *Journal of Geophysical Research*, *111*(E6), E06S24. https://doi.org/10.1029/2005JE002525

Holt, J. W., Truffer, M., Larsen, C. F., Christoffersen, M. S., & Tober, B. S. (2021). IceBridge ARES L1B geolocated radar echo strength profiles, version 1 [Dataset]. NASA National Snow and Ice Data Center DAAC. https://doi.org/10.5067/X2H7MP5DBTYP

Hugonnet, R., McNabb, R., Berthier, E., Menounos, B., Nuth, C., Girod, L., et al. (2021). Accelerated global glacier mass loss in the early twenty-first century. *Nature*, *592*(7856), 726–731. Article 7856. https://doi.org/10.1038/s41586-021-03436-z

Huss, M., & Farinotti, D. (2012). Distributed ice thickness and volume of all glaciers around the globe. *Journal of Geophysical Research*, *117*(F4), F04010. https://doi.org/10.1029/2012JF002523

Jacob, T., Wahr, J., Pfeffer, W. T., & Swenson, S. (2012). Recent contributions of glaciers and ice caps to sea level rise. *Nature*, *482*(7386), 514–518. https://doi.org/10.1038/nature10847

Kienholz, C., Rich, J. L., Arendt, A. A., & Hock, R. (2014). A new method for deriving glacier centerlines applied to glaciers in Alaska and northwest Canada. *The Cryosphere*, *8*(2), 503–519. https://doi.org/10.5194/tc-8-503-2014

Krimmel, R. M., & Meier, M. F. (1975). Glacier applications of Erts images. *Journal of Glaciology*, *15*(73), 391–402. https://doi.org/10.3189/S002214300003450X

Lapazaran, J. J., Otero, J., Martín-Español, A., & Navarro, F. J. (2016). On the errors involved in ice-thickness estimates I: Ground-penetrating radar measurement errors. *Journal of Glaciology*, *62*(236), 1008–1020. https://doi.org/10.1017/jog.2016.93

Larsen, C. (2020). IceBridge UAF lidar scanner L1B geolocated surface elevation triplets, version 1 [Dataset]. NASA National Snow and Ice Data Center Distributed Active Archive Center. https://doi.org/10.5067/AATE4JJ91EHC

Larsen, C. F., Burgess, E., Arendt, A. A., O'Neel, S., Johnson, A. J., & Kienholz, C. (2015). Surface melt dominates Alaska glacier mass balance. *Geophysical Research Letters*, *42*(14), 5902–5908. https://doi.org/10.1002/2015GL064349

MacGregor, J. A., Boisvert, L. N., Medley, B., Petty, A. A., Harbeck, J. P., Bell, R. E., et al. (2021). The scientific legacy of NASA's Operation IceBridge. *Reviews of Geophysics*, *59*(2), e2020RG000712. https://doi.org/10.1029/2020RG000712

MacKie, E. J., Schroeder, D. M., Zuo, C., Yin, Z., & Caers, J. (2021). Stochastic modeling of subglacial topography exposes uncertainty in water routing at Jakobshavn Glacier. *Journal of Glaciology*, *67*(261), 75–83. https://doi.org/10.1017/jog.2020.84

Maussion, F., Butenko, A., Champollion, N., Dusch, M., Eis, J., Fourteau, K., et al. (2019). The open global glacier model (OGGM) v1.1. *Geoscientific Model Development*, *12*(3), 909–931. https://doi.org/10.5194/gmd-12-909-2019

Millan, R., Mouginot, J., Rabatel, A., & Morlighem, M. (2022). Ice velocity and thickness of the world's glaciers. *Nature Geoscience*, *15*(2), 124–129. Article 2. https://doi.org/10.1038/s41561-021-00885-z

Molnia, B. (2001). U.S. Geological Survey professional paper 1386-K. Retrieved from https://pubs.usgs.gov/pp/p1386k/

Molnia, B. F., & Jones, J. E. (1989). View through ice. *Eos, Transactions American Geophysical Union*, *70*(28), 701–710. https://doi.org/10.1029/89EO00221

Motyka, R. J., Truffer, M., Kuriger, E. M., & Bucki, A. K. (2006). Rapid erosion of soft sediments by tidewater glacier advance: Taku Glacier, Alaska, USA. *Geophysical Research Letters*, *33*(24), L24504. https://doi.org/10.1029/2006GL028467

Moussessian, A., Jordan, R. L., Rodriguez, E., Safaeinili, A., Akins, T. L., Edelstein, W. N., et al. (2000). A new coherent radar for ice sounding in Greenland. In *IGARSS 2000. IEEE 2000 international geoscience and remote sensing symposium. Taking the pulse of the planet: The role of remote sensing in managing the environment. Proceedings (Cat. No.00CH37120)* (Vol. 2, pp. 484–486). https://doi.org/10.1109/IGARSS.2000.861604

Muskett, R. R., Lingle, C. S., Sauber, J. M., Post, A. S., Tangborn, W. V., & Rabus, B. T. (2008). Surging, accelerating surface lowering and volume reduction of the Malaspina Glacier system, Alaska, USA, and Yukon, Canada, from 1972 to 2006. *Journal of Glaciology*, *54*(188), 788–800. https://doi.org/10.3189/002214308787779915

Pavlis, T. L., Chapman, J. B., Bruhn, R. L., Ridgway, K., Worthington, L. L., Gulick, S. P. S., & Spotila, J. (2012). Structure of the actively deforming fold-thrust belt of the St. Elias orogen with implications for glacial exhumation and three-dimensional tectonic processes (Vol. *29*).

Pfeffer, W. T. (2007). A simple mechanism for irreversible tidewater glacier retreat. *Journal of Geophysical Research*, *112*(F3), F03S25. https://doi.org/10.1029/2006JF000590

Plafker, G. (1987). Regional geology and petroleum potential of the northern Gulf of Alaska continental margin. Retrieved from http://archives.datapages.com/data/circ_pac/0007/0229_f.htm

Post, A. (1969). Distribution of surging glaciers in Western North America. *Journal of Glaciology*, *8*(53), 229–240. https://doi.org/10.3189/S0022143000031221

Post, A., O'Neel, S., Motyka, R. J., & Streveler, G. (2011). A complex relationship between calving glaciers and climate. *Eos, Transactions American Geophysical Union*, *92*(37), 305–306. https://doi.org/10.1029/2011EO370001

Rasmussen, C. E., & Williams, C. K. (2006). *Gaussian processes for machine learning*. The MIT Press. Retrieved from www.GaussianProcess.org/gpml

Raup, B., Racoviteanu, A., Khalsa, S. J. S., Helm, C., Armstrong, R., & Arnaud, Y. (2007). The GLIMS geospatial glacier database: A new tool for studying glacier change. *Global and Planetary Change*, *56*(1), 101–110. https://doi.org/10.1016/j.gloplacha.2006.07.018

Rignot, E., Mouginot, J., Larsen, C. F., Gim, Y., & Kirchner, D. (2013). Low-frequency radar sounding of temperate ice masses in Southern Alaska. *Geophysical Research Letters*, *40*(20), 5399–5405. https://doi.org/10.1002/2013GL057452

Russell, I. C. (1893). Malaspina Glacier. *The Journal of Geology*, *1*(3), 219–245. https://doi.org/10.1086/606179

Sharp, R. P. (1951). Accumulation and ablation on the Seward-Malaspina Glacier system, Canada-Alaska. *GSA Bulletin*, *62*(7), 725–744. https://doi.org/10.1130/0016-7606(1951)62[725:AAAOTS]2.0.CO;2

Sharp, R. P. (1958). Malaspina Glacier, Alaska. *GSA Bulletin*, *69*(6), 617–646. https://doi.org/10.1130/0016-7606(1958)69[617:MGA]2.0.CO;2

Shi, L., Allen, C. T., Ledford, J. R., Rodriguez-Morales, F., Blake, W. A., Panzer, B. G., et al. (2010). Multichannel coherent radar depth sounder for NASA Operation Ice Bridge. In *2010 IEEE international geoscience and remote sensing symposium* (pp. 1729–1732). https://doi.org/10.1109/IGARSS.2010.5649518

Shreve, R. L. (1972). Movement of water in glaciers. *Journal of Glaciology*, *11*(62), 205–214. https://doi.org/10.3189/S002214300002219X

Swiler, L., Gulian, M., Frankel, A., Safta, C., & Jakeman, J. (2020). A survey of constrained Gaussian process regression: Approaches and implementation challenges. *Journal of Machine Learning for Modeling and Computing*, *1*(2), 119–156. https://doi.org/10.1615/JMachLearnModelComput.2020035155

Tarboton, D. G. (1997). A new method for the determination of flow directions and upslope areas in grid digital elevation models. *Water Resources Research*, *33*(2), 309–319. https://doi.org/10.1029/96WR03137

Thompson, A., Loso, M., Jones, T., Truffer, M., Holt, J., Devaux-Chupin, V., et al. (2021). Saltwater intrusion in proglacial lakes at Malaspina glacier, Southeast Alaska: Introducing the worlds newest tidewater glacier. 2021 (Vol. *C13B-07*).

Thompson, A. C., Loso, M. G., Mooneyham, S. A., Tober, B. S., Larsen, C. F., & Holt, J. W. (2023). Surficial Geology and Proglacial Lake Change at Sít' Tlein (recently known as "Malaspina Glacier"), Wrangell-St. Elias National Park and Preserve, Alaska. *Natural Resource Report NPS/WRST/NRR*—2023/XXXX. National Park Service, Fort Collins, Colorado.

Tober, B. S., & Christoffersen, M. S. (2022). Radar analysis graphical utility (RAGU) [Software]. Zenodo. https://doi.org/10.5281/zenodo.6366661

Truffer, M., Holt, J., Larsen, C., Christoffersen, M., & Tober, B. S. (2021). IceBridge UAF L1B HF geolocated radar echo strength profiles, version 1 [Dataset]. NASA National Snow and Ice Data Center DAAC. https://doi.org/10.5067/Q0AVPHN3250H

Truffer, M., Holt, J. W., Larsen, C. F., & Fahnestock, M. A. (2016). *High resolution bed topography for the Malaspina Glacier lobe* (Vol. 13). AGU Fall Meeting Abstracts. Retrieved from http://adsabs.harvard.edu/abs/2016AGUFM.C13C0836T

Walton, M. A., Gulick, S. P. S., & Haeussler, P. J. (2022). Revisiting the 1899 earthquake series using integrative geophysical analysis in Yakutat Bay, Alaska. *Geosphere*, *18*(3), 1453–1473. https://doi.org/10.1130/GES02423.1

Watts, R. D., & England, A. W. (1976). Radio-echo sounding of temperate glaciers: Ice properties and sounder design criteria. *Journal of Glaciology*, *17*(75), 39–48. https://doi.org/10.3189/S0022143000030707

Worthington, L. L., Avendonk, H. J. A. V., Gulick, S. P. S., Christeson, G. L., & Pavlis, T. L. (2012). Crustal structure of the Yakutat terrane and the evolution of subduction and collision in southern Alaska. *Journal of Geophysical Research*, *117*(B1), B01102. https://doi.org/10.1029/2011JB008493

Worthington, L. L., Gulick, S. P. S., & Pavlis, T. L. (2010). Coupled stratigraphic and structural evolution of a glaciated orogenic wedge, offshore St. Elias orogen, Alaska. *Tectonics*, *29*(6), TC6013. https://doi.org/10.1029/2010TC002723

Zechmann, J. M., Truffer, M., Motyka, R. J., Amundson, J. M., & Larsen, C. F. (2021). Sediment redistribution beneath the terminus of an advancing glacier, Taku Glacier (T'aakú Kwáan Sít'i), Alaska. *Journal of Glaciology*, *67*(262), 204–218. https://doi.org/10.1017/jog.2020.101

Zemp, M., Huss, M., Thibert, E., Eckert, N., McNabb, R., Huber, J., et al. (2019). Global glacier mass changes and their contributions to sea-level rise from 1961 to 2016. *Nature*, *568*(7752), 382–386. Article 7752. https://doi.org/10.1038/s41586-019-1071-0

Zurbuchen, J. M., Gulick, S. P. S., Walton, M. A. L., & Goff, J. A. (2015). Imaging evidence for Hubbard Glacier advances and retreats since the last glacial maximum in Yakutat and Disenchantment Bays, Alaska. *Geochemistry, Geophysics, Geosystems*, *16*(6), 1962–1974. https://doi.org/10.1002/2015GC005815

Erratum

The originally published version of this article contained a typographical error. In the first paragraph of Section 2.1, the sentence beginning "Operation IceBIB annually acquired . . ." has been corrected to "Operation IceBridge annually acquired . . . ." This version may be considered the authoritative version of record.